




Simulating high-realistic galaxy scale strong lensing in galaxy clusters to train deep learning methods

G. Angora^{1,2}, P. Rosati^{1,3,9}, M. Meneghetti³, M. Brescia^{2,4,12},
A. Mercurio^{2,10}, C. Grillo^{5,6}, P. Bergamini^{3,5}, A. Acebron^{5,6},
G. Caminha^{7,8}, L. Tortorelli¹¹, L. Bazzanini^{1,3} and E. Vanzella³

¹Dipartimento di Fisica e Scienze della Terra, Università di Ferrara, Via Saragat 1, I-44122 Ferrara, Italy. email: gius.angora@gmail.com

²INAF – Osservatorio Astronomico di Capodimonte, Salita Moiariello 16, I-80131 Napoli, Italy

³INAF – OAS, Osservatorio di Astrofisica e Scienza dello Spazio di Bologna, via Gobetti 93/3, I-40129 Bologna, Italy

⁴Dipartimento di Fisica “E. Pancini”, Università di Napoli “Federico II”, Via Cinthia 21, I-80126 Napoli, Italy

⁵Dipartimento di Fisica, Università di Milano, via Celoria 16, I-20133 Milano, Italy

⁶INAF – IASF Milano, via A. Corti 12, I-20133 Milano, Italy

⁷Technische Universität München, Physik-Department, James-Franck Str. 1, D-85741 Garching, Germany

⁸Max-Planck-Institut für Astrophysik, Karl-Schwarzschild-Str. 1, D-85748 Garching, Germany

⁹INFN, Sezione di Ferrara, Via Saragat 1, I-44122 Ferrara, Italy

¹⁰Dipartimento di Fisica, Università di Salerno, Via Giovanni Paolo II, 132, I-84084, Fisciano (SA), Italy

¹¹University Observatory, Faculty of Physics, Ludwig-Maximilians-Universität München, Scheinerstr. 1, D-81679 Munich, Germany

¹²INFN, Sezione di Napoli, Via Cinthia 21, I-80126 Napoli, Italy

Abstract. Galaxy-galaxy strong lensing in galaxy clusters is a unique tool for studying the sub-halo mass distribution, as well as for testing predictions from cosmological simulations. We describe a novel method that simulates realistic lensed features embedded inside the complexity of observed data by exploiting high-precision cluster lens models. Such methodology is used to build a large dataset with which Convolutional Neural Networks have been trained to identify strong lensing events in galaxy clusters. In particular, we inject lensed sources around cluster members using the images acquired by the Hubble Space Telescope. The resulting simulated mock data preserve the complexity of observation by taking into account all the physical components that could affect the morphology and the luminosity of the lensing events. The trained networks achieve a purity-completeness level of $\sim 91\%$ in detecting such events. The methodology presented can be extended to other data-intensive surveys carried out with the next-generation facilities.

Keywords. Gravitational lensing, galaxies: clusters, image processing, deep learning

1. Introduction

Strong gravitational lensing proves highly effective in studying the galaxies and galaxy clusters' mass distribution by also acting as a powerful tool to test cosmological models. For example, strong lensing has been used to: (i) estimate the Hubble constant exploiting time-delay measurements (e.g. [Suyu *et al.* 2017, 2020](#); [Grillo *et al.* 2018](#); [Millon *et al.* 2020](#); [Moresco *et al.* 2022](#)); (ii) constrain the dark energy equation of state (e.g. [Jullo *et al.* 2010](#); [Cao, Covone, & Zhu 2012](#); [Collett & Auger 2014](#); [Caminha *et al.* 2022](#)); (iii) estimate the dark matter fraction in massive early-type galaxies (e.g. [Grillo 2010](#); [Tortora *et al.* 2010](#); [Sonnenfeld *et al.* 2015](#)); (iv) test cosmological simulations and/or dark matter properties (e.g. [Meneghetti *et al.* 2020, 2022](#)); (v) analyze galaxy structures and their evolution (e.g. [Treu & Koopmans 2002](#); [Auger *et al.* 2010](#); [Sonnenfeld *et al.* 2013](#)); (vi) study lensed (magnified) high-redshift sources revealed by the cluster that acts as cosmic telescope ([Swinbank *et al.* 2009](#); [Richard *et al.* 2011](#); [Vanzella *et al.* 2020, 2021](#)). In addition, the total mass distribution of clusters can be studied with strong-lensing cluster-scaled models which exploit an increasing number of multiple images of background sources (e.g. [Caminha *et al.* 2017, 2019](#); [Acebron *et al.* 2018](#); [Bergamini *et al.* 2019, 2021, 2023](#); [Lagattuta *et al.* 2019, 2022](#)).

In this work, we explore the capabilities of deep learning methods to automatically search for galaxy–galaxy strong lenses (GGSLs) in galaxy clusters. In these environments, due to the large-scale contribution of the cluster, the probability of GGSLs is generally higher than in the field. Although these systems have been identified through visual inspection of candidates (e.g. [Le Fèvre & Hammer 1988](#); [Jackson 2008](#); [Sygnet *et al.* 2010](#); [Pawase *et al.* 2014](#)), in recent years deep learning techniques have been proven as an efficient method to solve this problem automatically (e.g. [Petrillo *et al.* 2017, 2019](#); [Metcalf *et al.* 2019](#); [Li *et al.* 2020, 2021](#); [Gentile *et al.* 2022](#); [Cañameras *et al.* 2021](#); [Akhazhanov *et al.* 2022](#)), preparing for the upcoming “Big Data Era” in astronomy inaugurated by the launch of the ESA satellite Euclid on July 2023 ([Laureijs *et al.* 2014](#)), together with the upcoming surveys carried out with next-generation facilities, such as the Vera Rubin Observatory ([Ivezić *et al.* 2019](#)). Indeed, deep learning methods, with their capabilities to search for hidden correlations within high-dimensional datasets, are able to successfully explore this huge amount of data in a few tens of seconds. Beyond this performative result, this work is focused on the main requirement (maybe the most important) for the training of deep learning techniques: the building of a suitable knowledge space (KB) based on which a convolutional neural network (CNN, [LeCun 1989, 1998](#)), can detect GGSL in the dense environment of galaxy clusters. Indeed, GGSLs are rare phenomena. For this reason, several efforts have been carried out in the last decades to simulate these events. For example, lens galaxies can be extracted from semi-analytical catalogs (e.g. with the Millennium Observatory project, as done by [Metcalf *et al.* 2019](#), or by [Leuzzi *et al.* 2023](#)) or by modeling the mass density profile of photometrically selected galaxies (e.g. [Petrillo *et al.* 2017, 2019](#); [Li *et al.* 2020, 2021](#); [Gentile *et al.* 2022](#); [Cañameras *et al.* 2021](#); [Akhazhanov *et al.* 2022](#)). On the other hand, lensed sources can be simulated by describing their surface brightness distributions (e.g. [Petrillo *et al.* 2017, 2019](#); [Li *et al.* 2020, 2021](#); [Gentile *et al.* 2022](#)) or directly sampled from observations (e.g. [Meneghetti *et al.* 2008, 2010](#); [Metcalf *et al.* 2019](#)) and then co-added to real or synthetic images through ray-tracing techniques (e.g. [GLAMER Metcalf & Petkova 2014](#); [Petkova *et al.* 2014](#), [GRAVLENS Keeton 2001](#)). However, in this work, we exploit a novel approach that simulates GGSLs in galaxy clusters by taking advantage of accurate cluster deflection fields provided by high-precision cluster lens models constructed by [Bergamini *et al.* \(2019, 2021\)](#) and [Caminha *et al.* \(2019\)](#). These models consider the cluster-scale and the subhalo (i.e. the cluster members, CLMs) mass components for

a given distribution of background sources. Thus, the GGSL simulation is driven by a realistic description of the CLMs, which behaves as though they actually were the lenses in lensing events, since the process takes into account all the physical components that could affect the morphology, the brightness, and the frequency of the events.

As aforementioned, this work focuses on the simulation methodology. All the details about the network implementations, the handling of train-test set splitting, together with a full description of the CNN performances and the analysis of the results can be found in [Angora et al. \(2020\)](#) and [Angora et al. \(2023\)](#). Thus, the paper extensively emphasizes the simulation process and the KB building in Section 2, by just summarizing the CNN results in Section 3; finally, we draw out conclusions in Section 4 and outline the future perspectives in Section 5.

Throughout the paper, we adopt a flat Λ CDM cosmological model with $\Omega_M=0.3$, $\Omega_\Lambda=0.7$, and $H_0=70\text{ km s}^{-1}\text{ Mpc}^{-1}$. All astronomical images are oriented north to the top and east to the left. Unless otherwise specified, magnitudes are in the AB system.

2. Simulating GGSLs in Hubble images: building the KB

The simulation exploits the deflection angle maps of eight galaxy clusters obtained from cluster lens models[†] provided by [Bergamini et al. \(2019, 2021\)](#) and [Caminha et al. \(2019\)](#). The cluster sample spans a redshift range between 0.234 and 0.587 (it is fully described in Table 1 of [Angora et al. 2023](#)). A complete description of the cluster-scale lensing modeling can be found in [Bergamini et al. \(2021\)](#), here we summarize the main points. The gravitational potential of each cluster is described through a parametric model which includes: (i) the cluster-scale components, i.e. dark matter halo and the smooth intracluster hot-gas mass (when available, e.g. [Bonamigo et al. 2017, 2018](#)), (ii) the clumpy terms associated to the CLMs; (iii) any further massive objects in the cluster outskirts or along the line of sight (LoS). We underline that the mass density profile of the subhalos is modeled with a circular, singular dual-pseudo isothermal profile ([Limousin, et al. 2005](#); [Elíasdóttir et al. 2007](#)), calibrated by measuring stellar velocity dispersions of a large sample of CLMs. Such lens models reproduce the observed positions of many multiple images (ranging from ~ 20 to ~ 200) with a typical accuracy of $\lesssim 0.5''$.

In this work, we inject GGSLs in three images acquired by the Hubble Space Telescope (HST) Advanced Camera for Survey (ACS), as part of the CLASH (Cluster Lensing And Supernova survey with Hubble, [Postman et al. 2012](#)) and HFF (Hubble Frontier Fields, [Lotz et al. 2017](#)) surveys. In particular, we exploit three ACS bands: F435W, F606W, and F814W. However, this process can be applied to any image, acquired with any kind of instrument as long as the related deflection field is available.

The simulation process is carried out by using a python package, `PyLensLib` ([Meneghetti 2022](#)). It is graphically depicted in Figure 1, and summarizes as follows.

- (0) Inputs: (i) the source, described as a Sérsic profile ([Sérsic 1963, 1968](#)) and with a star-forming galaxy spectral energy distribution (SED, [Kinney et al. 1996](#)), together with its intrinsic (F814W) magnitude and its redshift \ddagger ; (ii) the angle deflection maps (computed from the lens model given the source and lens redshift), $\vec{\alpha}$, which describes the relation between the source real position ($\vec{\beta}$) and the observed position $\vec{\theta}$ (see also right panels in Figure 1), through the lens equation:

$$\vec{\beta} = \vec{\theta} - \vec{\alpha} \quad (1)$$

[†] The cluster lens models are publicly available at <https://www.fe.infn.it/astro/lensing/>.

[‡] The adopted ranges of the Sérsic parameters can be found in Table 2 of [Angora et al. \(2023\)](#).

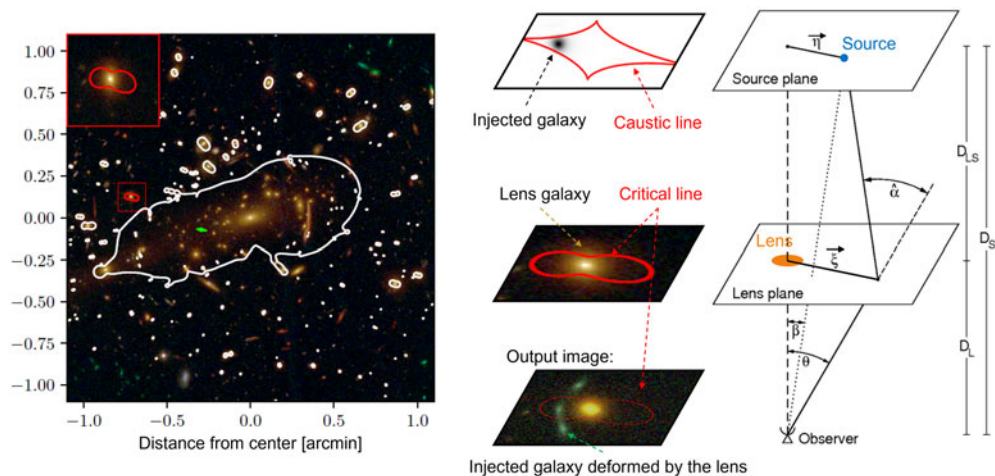


Figure 1. A flow chart representing the simulation process. *Left panel:* the cluster MACSJ 1206 with the critical lines (in white) at $z = 2.5$ from the lens model built by Bergamini *et al.* (2019), where a specific secondary critical line is selected (marked in red and zoomed-in the $10''$ inset axis). *Central panels:* the source is injected inside the caustic line corresponding to the selected critical line; the simulated GGSL is obtained through ray-tracing. *Right panels:* the corresponding geometric description of the lensing event.

- (1) The critical lines (on the lens plane, see the left panel in Figure 1) are computed from the deflection field by imposing that the magnification goes to infinity (the elements of the magnification tensor can be computed from the convergence and shear maps, i.e. the Jacobian matrix describing the image deformation).
- (2) a secondary critical line is randomly extracted inside an (equivalent) Einstein radius range: $\theta_E \in (0.2'', 3.5'')$ (prevent the sampling of the primary critical lines and very small-scaled galaxies). These limits are compatible with the expected Einstein radii distribution (see Figure 7 in Meneghetti *et al.* 2022).
- (3) The selected secondary critical line is mapped into the corresponding caustic line (on the source plane) using the lens equation 1 (see central panels in Figure 1). The source is injected within a buffer surrounding the caustic (whose width is a fraction of the source effective radius, $0.5r_e$).
- (4) Since the lens mapping preserves the surface brightness, i.e. $I(\vec{\theta}) = I(\vec{\beta})$, the resulting surface brightness on the lens plane is computed as $I(\vec{\theta} = \vec{\beta} + \vec{\alpha})$. Finally, the generated lensed system is convolved with the HST point spread function (PSF) and coadded to the HST image. In this work, the PSFs are estimated with `morphofit` (Tortorelli & Mercurio 2023).

In order to reproduce an observed Universe, the source intrinsic magnitude and redshift are extracted by exploiting the COSMOS 2015 catalog (Laigle *et al.* 2016) complemented with HST Deep Field North and South observations (Williams *et al.* 1996; Metcalfe *et al.* 2001). Specifically, we estimate the number counts (i.e. the number of galaxies per squared degree per magnitude bin) in F814W down to 29 mag, and we fit a redshift probability density function (PDF) in 6 magnitude bin, i.e. $p(z|\Delta m) = az^2e^{-(z/z_0)^b}$ (Lombardi & Bertin 1999; Lombardi *et al.* 2005, see also Figure 3 in Angora *et al.* 2023). In this way, we can extract a source magnitude (in the range 22 – 29) and, given this magnitude, a corresponding redshift. In the COSMOS 2015 catalog the photometric redshift limit is ~ 7 , which is suitable for our experiments since the reddest band is the

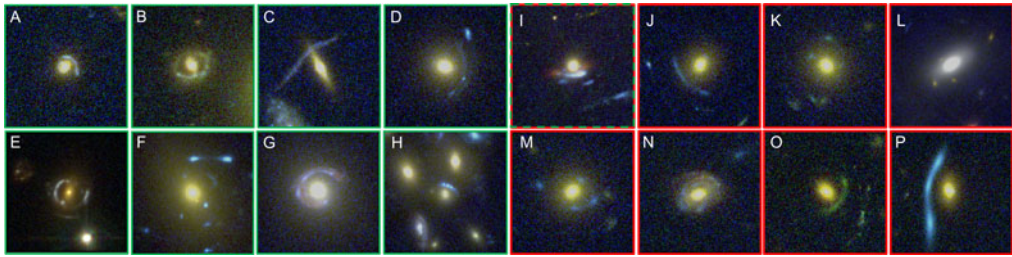


Figure 2. Comparison between real (in the left panels, with green edges) and simulated (in the right panels, with red edges) GGSLS. Note that in the panel *I* there is a combination of real and simulated events: the blue arc is a true GGSL (with a source at $z \sim 2$), whereas the red arc is injected ($z \sim 6$). *References.* Desprez *et al.* (2018): panels A, B, D, E and G; Diego *et al.* (2015): panel C; Smith *et al.* (2005): panels F and H, Caminha *et al.* (2016): panel I.

F814W. On the other hand, we set a minimum value for the source redshift equals to $z_{\text{src}} = z_{\text{cls}} + 0.4$, which is suggested by studying the lensing cross-section of galaxies in galaxy clusters (Meneghetti *et al.* 2022). Figure 2 shows a comparison between real and simulated GGSLS.

Finally, the building of KB is completed by selecting a pure sample of non-GGSL, i.e. the negative class in the dataset. Lensing experts in our group visually inspected thousand of cutouts centered on CLM centroids by excluding any thumbnail that contained strong lensing features. This result has been carried out by exploiting a large spectroscopic coverage part of the CLASH-VLT VIMOS (Rosati *et al.* 2014) program combined with MUSE archival observations (Bacon *et al.* 2012, 2014, 2015). The resulting non-GGSL sample comprises of ~ 1500 objects. Therefore, the GGSL set in the KB is composed of ~ 3000 events, i.e. two times the number of non-GGSLS, with the aim to ensure a large variety of lensing mock examples. This intentional mismatch is balanced during the augmentation pre-processing phase, which leads to a balanced training set of ~ 3800 images for each class. Cutouts have a side of 128×128 pixels (i.e. $3.84''$ by side).

3. Classification performances

The CNN classification performances have been measured with a set of metrics that can be computed from the binary confusion matrix: the average efficiency (*AE*), purity (*pur*), completeness (*compl*), and the *F1* - score. These estimators can completely describe the CNN capability to disentangle the GGSLS from the negative class. In particular, the *AE* is a global score measured by combining both classes, while the others refer to each class: *pur* is related to the degree of contamination in the network predicted sample, *compl* is the capability to identify *all* the sources, the *F1* is the harmonic mean between purity and completeness, which has been included to take into account the typical dichotomy between these estimators.

We tested several CNN architectures; here, we summarize the results achieved by the two best networks. The first is inspired by the work of Simonyan & Zisserman (2014), a VGG-like (Visual Group Geometry) network. The second architecture was implemented based on a posterior analysis of the results, it consists of three parallel networks, each of them processes a single channel, for this reason, we named it SC-VGG. All the details about these networks can be found in Angora *et al.* (2020, 2023).

Table 1 compares the classification performances of the two networks in terms of the adopted statistical estimators. Moreover, we tested the CNN capabilities to identify GGSLS by exploiting just a band (last three columns in Table 1). Globally speaking, all the studied configurations are purer than complete with respect to the identification

Table 1. Classification performance comparison.

	[%]	VGG	SC-VGG	F435W	F606W	F814W
	AE	87.7	89.4	87.2	86.1	86.8
GGSL	<i>pur</i>	93.4	93.1	91.8	91.1	91.5
	<i>compl</i>	88.6	91.7	89.8	88.8	89.3
	<i>F1</i>	91.0	92.4	90.8	89.9	90.4
non-GGSL	<i>pur</i>	76.7	81.4	77.5	75.4	76.6
	<i>compl</i>	85.4	84.1	81.3	79.9	80.9
	<i>F1</i>	81.1	82.8	79.3	77.6	78.7

Notes: Beyond the comparison between the two architectures, we show the results achieved by networks trained with a single band (last three columns).

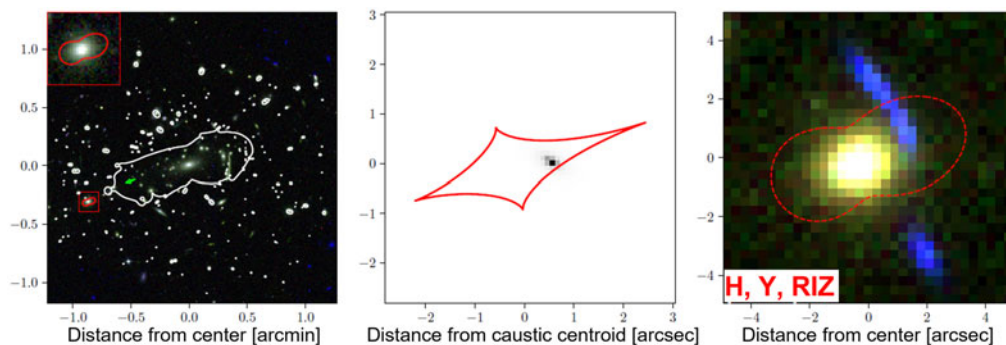


Figure 3. Simulation process in an euclidized image. *Left panel:* the euclidized FoV of the cluster MACS J1206, together with the critical lines. The selected secondary critical line is in red and is also shown in the upper-left inset axis. *Central panel:* the corresponding caustic (on the source plane at $z = 1.5$) with the source ($\text{mag}_{\text{RIZ}} = 23.0$). *Right panel:* the resulting GGSLs as a color-composite image.

of GGSLs, with purity measures ranging in $91.1 - 93.4$; whereas the completeness fluctuation range is lower ($88.6 - 91.7$). Opposite behavior regarding the non-GGSL class. The SC-VGG shows more stable results for both classes by achieving the highest *F1*-scores. This is due to its capability to identify better high- z GGSLs since it is not affected by the dropout problem (see the discussion in Angora *et al.* 2023).

Interestingly, we find that the network is able to classify GGSLs by also using just one band, even if with performance lower than those achieved by combining the three filters. It is not surprising that the best performances are carried out by using the bluer band (F435W). Although this filter has a lower signal-to-noise ratio, the network exploits the higher contrast between the lens (redder) and the lensed source (typically bluer).

4. Conclusion

In this work we outline the methodology with which a large dataset can be built to train CNNs in order to identify GGSL in galaxy clusters. The presented simulation process takes advantage of high-precision cluster deflection fields, which have been used to generate high-realistic mock lensed features embedded in the cluster environment. The resulting dataset reproduces the complexity of the lensing phenomenon by considering all the physical components that characterize the lenses. The implemented CNNs are able to classify GGSLs with a purity-completeness trade-off $\sim 91\%$.

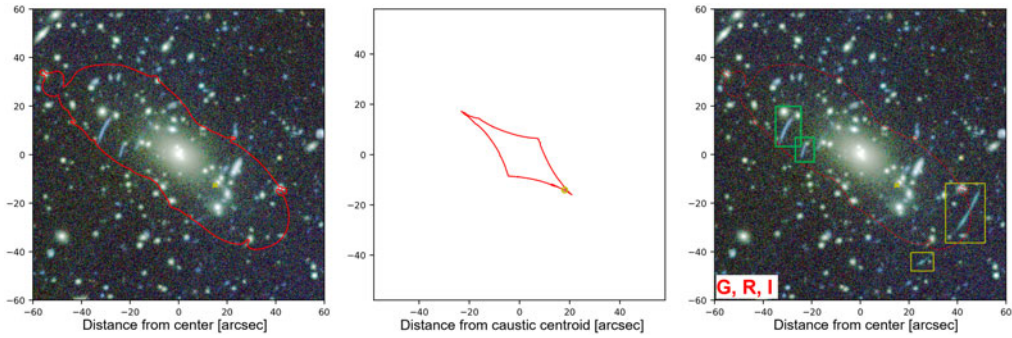


Figure 4. Cluster-scale simulation process in VST simulated image. *Left panel:* the VST FoV of the cluster RX J2248, together with the primary critical lines. *Central panel:* the corresponding caustic (on the source plane at $z = 2.9$) where the source location is shown as a yellow circle ($\text{mag}_{\text{RIZ}} = 25.0$). *Right panel:* the resulting simulated arcs (in yellow boxes) as a color-composite image. As comparison, two real arcs are enclosed by green boxes.

5. Future perspectives

This methodology has been tested with images acquired by the HST. Currently, we are extending this process to other instruments. For example, Figure 3 shows a simulated GGSL injected in the *euclidized* version of the HST FoV of the cluster MACS J1206. The euclidization has been carried out with the tool HST2EUCLID (Bergamini et al. in prep.).

In addition, the same process can be exploited to simulate extended arc-like structures on a cluster scale. We are simulating thousands of arcs by injecting sources near the primary critical line. We plan to search for extended arcs in images acquired by the VLT Survey Telescope (VST). In order to exploit the high-precision cluster deflection maps (whose cluster lens models have been built with HST images), we implemented a tool that transforms HST images into VST mock data. The simulation process (graphically represented in Figure 4) is similar to that described in this work. In particular, in order to obtain high-magnified lensed arcs, we select the regions where the magnification is higher than 70. The right panel in Figure 4 shows a comparison between the injected arc (inside yellow boxes) and two observed arcs (inside green boxes).

References

- Acebron, A., Cibirka, N., Zitrin, A., et al. 2018, *Apj*, 858, 42.
 Akhazhanov, A., More, A., Amini, A., et al. 2022, *MNRAS*, 513, 2407.
 Angora, G., Rosati, P., Brescia, M., et al. 2020, *A&A*, 643, A177.
 Angora, G., Rosati, P., Meneghetti, M., et al. 2023, *A&A*, 676, A40.
 Auger, M.W., Treu, T., Gavazzi, R., et al. 2010, *Apj*, 721, L163.
 Bacon, R., Accardo, M., Adjali, L., et al. 2012, *The Messenger*, 147, 4.
 Bacon, R., Vernet, J., Borisova, E., et al. 2014, *The Messenger*, 157, 13.
 Bacon, R., Brinchmann, J., Richard, J., et al. 2015, *A&A*, 575, A75.
 Bergamini, P., Rosati, P., Mercurio, A., et al. 2019, *A&A*, 631, A130.
 Bergamini, P., Rosati, P., Vanzella, E., et al. 2021, *A&A*, 645, A140.
 Bergamini, P., Agnello, A., and Caminha, G.B. 2021, *A&A*, 648, A123.
 Bergamini, P., Acebron, A., Grillo, C., et al. 2023, *Apj*, 952, 84.
 Bonamigo, M., Grillo, C., Ettori, S., et al. 2017, *Apj*, 842, 132.
 Bonamigo, M., Grillo, C., Ettori, S., et al. 2018, *Apj*, 864, 98.
 Caminha, G.B., Grillo, C., Rosati, P., et al. 2016, *A&A*, 587, A80.
 Caminha, G.B., Grillo, C., Rosati, P., et al. 2017, *A&A*, 607, A93.
 Caminha, G.B., Rosati, P., Grillo, C., et al. 2019, *A&A*, 632, A36.
 Caminha, G.B., Suyu, S.H., Grillo et al. 2022, *A&A*, 657, A83.

- Cañameras, R., Schuldt, S., Shu, Y., *et al.* 2021, *A&A*, 653, L6.
- Cao S., Covone G., Zhu Z.H. 2012, *ApJ*, 755, 31.
- Collett, T.E. and Auger, M.W. 2014, *MNRAS*, 443, 969.
- Desprez, G., Richard, J., Jauzac, M., *et al.* 2018, *MNRAS*, 479, 2630.
- Diego, J.M., Broadhurst, T., Benitez, N., *et al.* 2015, *MNRAS*, 449, 588.
- Elíasdóttir, Á., Limousin, M., Richard, J., *et al.* 2007, *arXiv e-prints*, arXiv:0710.5636.
- Gentile, F., Tortora, C., Covone, G., *et al.* 2022, *MNRAS*, 510, 500.
- Grillo, C. 2010, *Apj*, 722, 779.
- Grillo, C., Rosati, P., Suyu, S.H., *et al.* 2018, *ApJ*, 860, 94.
- Ivezić, Ž., Kahn, S.M., Tyson, J.A., *et al.* 2019, *Apj*, 873, 111.
- Jackson, N. 2008, *MNRAS*, 389, 1311.
- Jullo, E., Natarajan, P., Kneib, J.-P., *et al.* 2010, *Science*, 329, 924.
- Keeton, C.R. 2001, *arXiv e-prints*, astro-ph/0102340.
- Kinney, A.L., Calzetti, D., Bohlin, R.C. *et al.* 1996, *Apj*, 467, 38.
- Lagattuta, D.J., Richard, J., Bauer, F.E., *et al.* 2019, *MNRAS*, 485, 3738.
- Lagattuta, D.J., Richard, J., Bauer, F.E., *et al.* 2022, *MNRAS*, 514, 497.
- Laigle, C., McCracken, H.J., Ilbert, O., *et al.* 2016, *Apjs*, 224, 24.
- Laureijs, R., Hoar, J., Buenadicha, G., *et al.* 2014, *Astronomical Data Analysis Software and Systems XXIII*, 485, 495.
- LeCun, Y., Boser, B., Denker, J. S., *et al.* 1989, *Neural Comput*, 1 (4), 541–551.
- Lecun, Y., Bottou, L., Bengio, Y., *et al.* 1998, *Proceedings of the IEEE* 86, 11, 2278–2324.
- Le Fèvre, O. and Hammer, F.: 1988, *Apj*, 333, L37.
- Leuzzi, L., Meneghetti, M., Angora, G., and Euclid Collaboration 2023, *arXiv e-prints*, arXiv:2307.08736.
- Li, R., Napolitano, N.R., Tortora, C., Spiniello, C., *et al.* 2020, *Apj*, 899, 30.
- Li, R., Napolitano, N.R., Spiniello, C., *et al.* 2021, *Apj*, 923, 16.
- Limousin, M., Kneib, J.-P., and Natarajan, P. 2005, *MNRAS*, 356, 309.
- Lombardi, M. and Bertin, G. 1999, *A&A*, 342, 337.
- Lombardi, M., Rosati, P., Blakeslee, J.P., *et al.* 2005, *Apj*, 623, 42.
- Lotz, J.M., Koekemoer, A., Coe, D., *et al.* 2017, *Apj*, 837, 97.
- Meneghetti, M., Melchior, P., Grazian, A., *et al.* 2008, *A&A*, 482, 403.
- Meneghetti, M., Rasia, E., Merten, J., *et al.* 2010, *A&A*, 514, A93.
- Meneghetti, M., Davoli, G., Bergamini, P., *et al.* 2020, *Science*, 369, 1347.
- Meneghetti, M. 2022, *Springer*, ISBN: 3-030-73582-6.
- Meneghetti, M., Ragagnin, A., Borgani, S., *et al.* 2022, *A&A*, 668, A188.
- Metcalfe, N., Shanks, T., Campos, A., *et al.* 2001, *MNRAS*, 323, 795.
- Metcalf, R.B. and Petkova, M. 2014, *MNRAS*, 445, 1942.
- Metcalf, R.B., Meneghetti, M., Avestruz, C., *et al.* 2019, *A&A*, 625, A119.
- Millon, M., Galan, A., Courbin, F., *et al.* 2020, *A&A*, 639, A101.
- Moresco, M., Amati, L., Amendola, L., *et al.* 2022, *Living Reviews in Relativity*, 25, 6.
- Pawase, R.S., Courbin, F., Faure, C., *et al.* 2014, *MNRAS*, 439, 3392.
- Petkova, M., Metcalf, R.B., and Giocoli, C. 2014, *MNRAS*, 445, 1954.
- Petrillo, C.E., Tortora, C., Chatterjee, S., *et al.* 2017, *MNRAS*, 472, 1129.
- Petrillo, C.E., Tortora, C., Vernardos, G., *et al.* 2019, *MNRAS*, 484, 3879.
- Postman, M., Coe, D., Benítez, N., *et al.* 2012, *Apjs*, 199, 25.
- Richard, J., Kneib, J.-P., Ebeling, H., *et al.* 2011, *MNRAS*, 414, L31.
- Rosati, P., Balestra, I., Grillo, C., *et al.* 2014, *The Messenger*, 158, 48.
- Sérsic, J.L. 1963, *Boletín de la Asociación Argentina de Astronomía La Plata Argentina*, 6, 41.
- Sérsic, J.L. 1968, *Cordoba, Argentina: Observatorio Astronómico, 1968*.
- Simonyan, K. and Zisserman, A. 2014, *arXiv e-prints*, arXiv:1409.1556.
- Smith, G.P., Kneib, J.-P., Smail, I., *et al.* 2005, *MNRAS*, 359, 417.
- Sonnenfeld, A., Treu, T., Gavazzi, R., *et al.* 2013, *Apj*, 777, 98.
- Sonnenfeld, A., Treu, T., Marshall, P.J., *et al.* 2015, *Apj*, 800, 94.
- Suyu, S.H., Bonvin, V., Courbin, F., *et al.* 2017, *MNRAS*, 468, 2590.

- Suyu, S.H., Huber, S., Cañameras, R., *et al.* 2020, *A&A*, 644, A162.
Swinbank, A.M., Webb, T.M., Richard, J., *et al.* 2009, *MNRAS*, 400, 1121.
Sygnet, J.F., Tu, H., Fort, B., *et al.* 2010, *A&A*, 517, A25.
Tortora, C., Napolitano, N.R., Romanowsky, A.J., and Jetzer, P. 2010, *Apj*, 721, L1.
Tortorelli, L. and Mercurio, A. 2023, *Frontiers in Astronomy and Space Sciences*, 10, 51.
Treu, T. and Koopmans, L.V.E. 2002, *Apj*, 575, 87.
Vanzella, E., Meneghetti, M., Caminha, G.B., *et al.* 2020, *MNRAS*, 494, L81.
Vanzella, E., Caminha, G.B., Rosati, *et al.* 2021, *A&A*, 646, A57.
Williams, R.E., Blacker, B., Dickinson, M., *et al.* 1996, *Apj*, 112, 1335.